

Fermi-pressure-assisted cavity superradiance in a mesoscopic Fermi gas

Francesca Orsi, Ekaterina Fedotova, Rohit Prasad Bhatt, Mae Eichenberger, Léa Dubois, and Jean-Philippe Brantut

*Institute of Physics and Center for Quantum Science and Engineering,
Ecole Polytechnique Fédérale de Lausanne (EPFL), Lausanne, Switzerland*

(Dated: March 10, 2026)

We study the superradiant phase transition of a mesoscopic Fermi gas comprising between a few tens and a few thousand ${}^6\text{Li}$ atoms in a high-finesse cavity across a wide range of densities. We observe a non-monotonic variation of the superradiant threshold as a function of density, with a minimum reached when the Fermi and recoil wavevectors are comparable. The minimum corresponds to a crossover between Fermi pressure-assisted ordering and Pauli blocking of photon scattering, in good agreement with theory. This interpretation is confirmed by a study of the atom-number dependence of the ordering threshold and photon number scaling. Lastly, we demonstrate the operation of our mesoscopic system in a regime where light-induced forces are opposite for the two spin components, leading to an ordered phase with a spin-density-wave character. Our system opens the perspective of studying few-fermion systems with strong and coherent light-matter coupling.

The interplay of Fermi statistics with interactions is at the heart of our understanding of the microscopic world, from the stability of matter to the chemical properties or optical spectrum of elements. In a system of degenerate Fermions subjected to an external drive, scattering processes can be suppressed by phase-space occupation constraints imposed by the Pauli principle, like in neutron scattering in solids or liquid Helium three [1]. In quantum gases, a paradigmatic example is the suppression of light scattering in a quantum-degenerate Fermi gas where photon recoil is Pauli blocked, which was predicted thirty years ago [2–4], and only recently observed experimentally [5–8].

The setting of cavity quantum-electrodynamics (QED) provides the cleanest platform to investigate the interplay between light-matter interactions and atomic motion. Compared with free-space scattering, it isolates a single mode of the electromagnetic field, which can then be monitored and controlled with exquisite precision [9–11]. Most importantly, the cavity feeds the light scattered by an atom back onto its emitter, leading to strong nonlinearities capable of driving a gas into a distinct, superradiant phase of matter [12–18], observed recently for degenerate Fermi gases [16, 17]. It was found that, in a deep one-dimensional optical lattice, the atom-number scaling of the superradiance threshold exhibits signatures of Pauli exclusion, with a reduced power-law exponent in a degenerate gas compared with a thermal gas [16]. For interacting systems, the threshold was observed to increase as the system crosses over from a Bose-Einstein condensate of molecules to a Bardeen-Cooper-Schrieffer superfluid, suggesting a role for Fermi statistics in hindering light scattering processes [17]. However so far Fermi statistics was only observed to suppress superradiance, in contrast with earlier predictions suggesting enhancement compared with a Bose-Einstein condensate in certain parameter regimes [19–22].

In this letter, we systematically study the role of Pauli blocking in the cavity-induced superradiant transition in a three-dimensional mesoscopic Fermi gas using a novel cavity-microscope system combining a high-finesse cavity with a micrometer-scale tweezer trap. The setup allows for variations of the atomic density over two orders of magnitudes at fixed atom number, yielding a Fermi sea with varying

radius. We find a non-monotonic threshold with a minimum when the recoil approaches twice the Fermi wavevector, in agreement with theory, a striking manifestation of the role of Fermi statistics in cavity superradiance. Our setup also allows to observe cavity superradiance with varying atom number between a few tens up to thousands, an uncharted regime between experiments with few individual, thermal atoms in tweezers [18, 23] and the regime of bulk, macroscopic quantum gases [12–18]. This capability enables the operation in the dispersive regime where the two spin components of the gas feel opposite light-induced forces, leading to an organized phase with an Ising spin-density wave character.

Cavity-induced superradiance originates from photon scattering between the cavity mode and a pump beam, yielding four discrete recoil momenta determined by the laser wavelength and the geometry, illustrated in Figure 1a. At low densities where atoms only populate low momenta, the associated energy cost is the photon recoil energy, and superradiance is similar than in Bose-Einstein condensates [13]. When density increases, Fermi pressure forces atoms to populate higher momentum states. As a result, photon scattering can occur at a reduced energy cost by going across the Fermi sea, as shown in Fig. 1b. This effect is distinct from Fermi surface nesting that was predicted to lead to thresholdless superradiance [19–21, 24, 25], and relies on the width of the momentum distribution rather than on its exact shape. It is thus more robust to experimental imperfections such as finite temperature or inhomogeneities. Upon further increasing the density, recoil processes become Pauli-excluded and photon scattering is suppressed (Fig. 1c), leading for example to sub-linear scaling of the threshold with atom number [16]. This behavior at zero-temperature is in sharp contrast with the case of weakly-interacting Bose-Einstein condensates, which displays no density dependence.

Our setup builds upon a cavity microscope described in [26] and consists of a Fabry-Perot cavity and a confocal lens pair sharing a common optical axis. As shown in Fig. 1d, the system comprises a pair of identical mirrors forming a near-concentric cavity, with high-reflectivity at 671 nm, the main dipole-allowed transition of ${}^6\text{Li}$, and at 1342 nm, providing an intracavity optical dipole trap [27]. The mirror coatings feature a high-transmission window around 765 nm, allowing

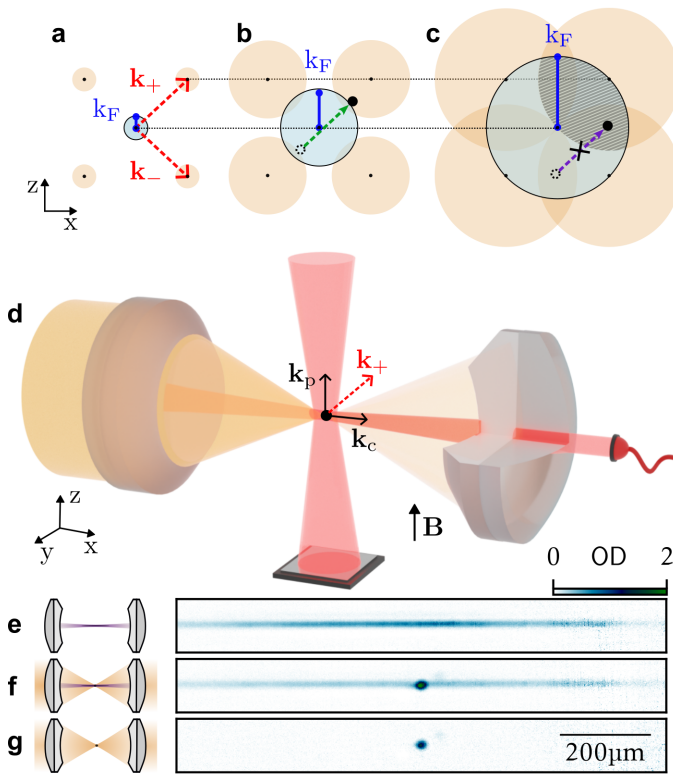


FIG. 1. Concept of the experiment. (a) Recoil processes involved in the scattering from a pump laser into a cavity and vice versa at wavevectors $\pm\mathbf{k}_{\pm}$ (---), compared with the radius k_F of the Fermi surface, at low (a), intermediate (b), and high density (c). (---) shows an example process at \mathbf{k}_+ favored by the existence of the Fermi sea, and (---) and example of Pauli-blocked \mathbf{k}_+ process. In (c), these processes correspond to the overlap between the Fermi sea (blue) and the Fermi sea displaced by $\pm\mathbf{k}_{\pm}$ (orange). (d) Cavity-microscope system comprising two mirrors contacted to aspherical lenses allowing to focus a tweezers trap (orange) onto an atomic cloud at the center of the cavity. The cavity mode with wavevector \mathbf{k}_c (red) shares the same optical axis as the tweezers trap beam. A retro-reflected transverse pump beam with wavevector $\mathbf{k}_p \perp \mathbf{k}_c$ (red) drives the atoms. Photons leaking through one of the cavity mirrors are detected on a single-photon counter. (e-g) Absorption images of atoms in state $|\downarrow\rangle$ after evaporation in the cavity-dipole trap alone (purple, not shown in panel (d)), (e), in the cavity-dipole trap superimposed with the tweezers trap (f), and after releasing the cavity dipole trap, yielding about $N = 4000$ atoms in the tweezers (g).

tight optical-tweezer trapping of the atoms in the center of the cavity mode using the full available numerical aperture of 0.34.

The sample preparation follows standard laser cooling and evaporative cooling in a cavity-assisted dipole trap [27] at the magnetic field of 316 G, yielding a cold mixture of the first and third hyperfine levels (labeled $|\downarrow\rangle$ and $|\uparrow\rangle$). Figure 1e shows a typical absorption image of the cloud produced after this step, with a temperature of $T/T_F = 1.1$ and a total atom number $N = 3 \times 10^4$. Performing the same evaporation procedure in the dipole trap in the presence of a tweezers trap at 765 nm tightly focused at the center of the cavity

yields about 4000 atoms in the tweezers on top of an extended ultracold gas, as can be seen in Fig. 1f. The tweezers has a trap depth of $10 \mu\text{K}$, a transverse trap frequency of 40 kHz and a beam waists of about $0.95 \mu\text{m}$ estimated from the trap frequency ratio. Thermal equilibrium in the combined trap yields an expected 100-fold decrease in T/T_F at the center of the tweezers [28, 29]. We then turn off the dipole trap (Figure 1g) and ramp down the tweezers-trap power to a variable set point to achieve the desired atom number. This procedure allows us to prepare atomic clouds with $40 < N < 2100$ in a balanced mixture of $|\uparrow\rangle, |\downarrow\rangle$. We find that the atom number remains unchanged if the bias magnetic field is first ramped to 566 G, where the scattering length is near zero [30], indicating that the tweezers-trap ramp primarily induces controlled spilling of an already highly degenerate quantum gas.

We investigate cavity superradiance by sending a retro-reflected, transverse pump laser beam with wavevector \mathbf{k}_p , polarized perpendicularly to the cavity axis. The beam intersects the cavity axis at a 90° angle at the location of the atoms, creating a lattice potential with depth V_0 . The atoms scatter light from the pump beam into the cavity field and back, yielding recoils at wavevectors $\pm\mathbf{k}_{\pm} = \pm\mathbf{k}_c \pm \mathbf{k}_p$, $k_{\pm} = |\mathbf{k}_{\pm}| = \sqrt{2}|\mathbf{k}_c|$, where \mathbf{k}_c is the cavity wavevector, as sketched in Figure 1d. The atoms undergo a superradiant phase transition when V_0 exceeds a critical value V_{0c} , corresponding to the emergence of a macroscopic density-wave in the gas at $\pm\mathbf{k}_{\pm}$ and the simultaneous buildup of a macroscopic field amplitude in the cavity. The level configuration and laser detunings are presented in Fig. 2a. The pump laser is red-detuned from the TEM_{00} mode of the cavity resonance by $\omega_c - \omega_p = \Delta_p = 2\pi \times 1.2 \text{ MHz}$, and from the atomic transition by $\Delta_{\uparrow} = \omega_{\uparrow} - \omega_p = 2\pi \times 300 \text{ MHz}$ with respect to the $|\uparrow\rangle \rightarrow |2P_{3/2} m_J = -3/2\rangle$ transition at 316 G. Here, V_0 is the depth felt by atoms in state $|\uparrow\rangle$, which is twice larger than for atoms in state $|\downarrow\rangle$ due to the relative detunings.

Following the preparation of a mesoscopic gas, the pump laser is abruptly turned on at a strength V_0 and the total number of photons N_{ph} leaking through one of the cavity mirrors within $30 \mu\text{s}$ is recorded. To observe the effect of Fermi pressure on the transition, we repeat these measurements varying the tweezers trap depth over about two-orders of magnitude after sample preparation, hence the trap frequencies over one order of magnitude, keeping the atom number fixed at $N = 48 \pm 36$ (see [27] for details on atom numbers). This compression varies the Fermi wavevector k_F continuously between $0.33 k_{\pm}$ and $1.33 k_{\pm}$, with $k_F = \sqrt{2mE_F}/\hbar$, $E_F = (3N)^{1/3}\hbar\bar{\omega}$, and $\bar{\omega}$ the geometric mean of the frequencies of the tweezers trap. The results are shown in Figure 2b. The raw photon counts are presented in logarithmic scale, together with the transition threshold inferred from the photon counts [27]. The superradiant threshold first decreases as the trap depth is increased, reaching a broad minimum before increasing again for the tightest confinements, manifesting the transition between free-space, Fermi-pressure-enhanced and Pauli-blocked superradiance.

We now confirm this interpretation by quantitatively

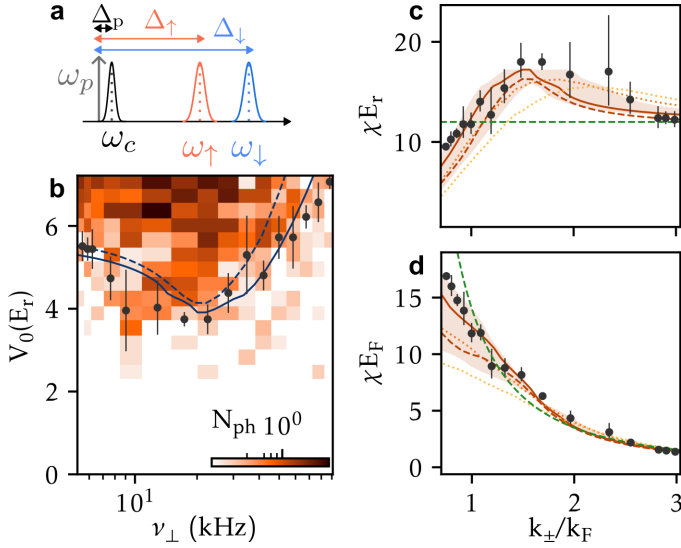


FIG. 2. Superradiant phase transition varying atomic density. (a) The two spin components $|\downarrow\rangle, |\uparrow\rangle$ interact with the cavity with resonance frequency ω_c and are driven by the pump field at frequency ω_p . (b) Photon number N_{ph} detected within $30\mu\text{s}$ following a quench of the pump laser power to V_0 , with varying trap frequency. Unless otherwise stated, all uncertainties on atom number represent 68% confidence interval on the mean, estimated using a resampling method [27]. Black points indicate the extracted thresholds. Error bars represent the standard deviation obtained by varying the critical photon number by $\pm 30\%$ [27]. Solid and dashed lines show theoretical predictions using the local density approximation (—) and exact harmonic-oscillator eigenstates (---). Each datapoint is averaged 9 times. (c) Normalized susceptibility extracted from the threshold as a function of the reduced wavevector k_{\pm}/k_F , showing a local maximum near $k_{\pm}/k_F \sim 1.7$. The experimental data are compared to theory with zero-temperature LDA (—) and exact eigenstates (---), as well as finite-temperature LDA theory for $T/T_F = 0.3$ (---) and 0.5 (---) and with the predictions for a Bose-Einstein condensate (---). The shaded area represents the effect of atom-number uncertainties on the zero-temperature LDA. (d) Susceptibility normalized by Fermi energy, compared with the same susceptibility predictions of panel (c).

comparing our observations to theory. To this end, we model the atoms as a harmonically trapped Fermi gas at finite temperature, dispersively coupled to the single-mode cavity in the presence of an external pump. We perform a linear stability analysis developed for quench protocols in [27, 31, 32], leading to the following equation for the critical pump potential:

$$V_{0c} = \frac{\tilde{\Delta}_p^2 + (\frac{\kappa}{2})^2}{\tilde{\Delta}_p} \frac{1}{2\chi U_0(1 + \zeta^2)} \quad (1)$$

where $\tilde{\Delta}_p$ is the detuning of the pump with respect to the cavity resonance, corrected from the bare detuning Δ_p by the atoms-induced dispersive shift, $U_0 = g^2/\Delta_{\uparrow}$ is the dipole potential created by one photon in the cavity and κ is the cavity intensity decay rate. The factor $(1 + \zeta^2)$ accounts for the unequal light-matter coupling of the two different spin components [27]. V_{0c} is the value of the pump potential V_0

that triggers the phase transition. It is expressed in terms of χ , the susceptibility measuring the linear response of the atomic density to the optical excitation at the wavevectors $\pm\mathbf{k}_{\pm}$. In our regime, accounting for the two different spin components and polarization effects, it can be traced down to the finite momentum, zero-frequency density-density response of the Fermi gas described by the Lindhard function [33]. Using our experimental parameters and performing trap averaging with the local-density approximation (LDA) yields a theoretical prediction for the zero-temperature threshold, shown as the solid line in Fig. 2b-d. Here the pump strength V_0 is calibrated using the weakest tweezer trap data, where the threshold is expected to be independent of quantum statistics or density. We find that it deviates by 40% from a direct estimate based on the beam profile, laser power and atomic polarizability. For these weak trap data, anharmonic effects in the tweezer which may lead to a systematic overestimate of the Fermi wavevector do not influence the physics.

The results are in good agreement with our experimental observations. In particular, the occurrence and location of the broad minimum in the threshold is accurately reproduced. We can use the threshold observed in our data to infer the susceptibility as a function of the reduced parameter k_{\pm}/k_F , as shown in Fig. 2c, with the susceptibility normalized by the recoil energy $E_r = \hbar^2 k_{\pm}^2/2m$. There we also present LDA results at finite temperature, where the maximum lowers

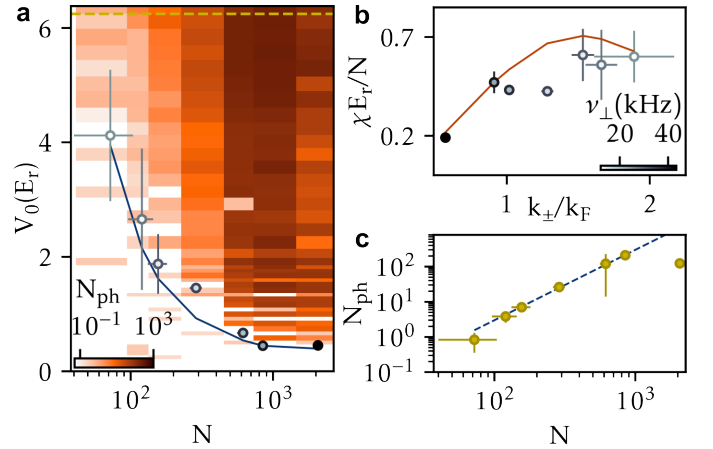


FIG. 3. Superradiant phase transition varying atom number. (a) Photon number with varying atom number within $70 \leq N < 2100$ for $\Delta_r/2\pi = 400$ MHz, $\tilde{\Delta}_p/2\pi = 1.3$ MHz. For each atom number the trap depth was adapted, with a value depicted using the grey scale. We overlap the measurement with the theory predictions (—) based on LDA simulation at zero temperature. The data is averaged between 2 and 10 times, depending on the signal-to-noise ratio. (b) Normalized susceptibility per atom extracted from the thresholds, compared with LDA predictions (—), demonstrating the universality of the behavior shown in Figure 2c. (c) Number of collected photons as a function of atom number for $V_0 = 6.2 E_r$ (--- horizontal cut in panel (a)), for which the threshold is exceeded for all atom numbers. Error bars on the photon number represent the standard deviation of the mean, calculated from different experimental repetitions. The dashed line is a guide to the eye showing the expected superradiant scaling $N_{\text{ph}} \propto N^2$.

and shifts to higher wavevectors due to the redistribution of momentum states occupation. The best agreement with our data is found for the zero temperature curve, providing an indirect confirmation of the low temperature of our mesoscopic Fermi gas. In the high-density regime (low k_{\pm}/k_F), the suppression is due to superradiance competing with Fermi pressure. In fact, at higher temperature, an increase of the threshold persists when the recoil energy is much smaller than temperature [27, 34]. This behavior is in sharp contrast with the prediction for a Bose-Einstein condensate, where the susceptibility of the gas corresponds to the recoil energy regardless of its density.

For our low atom number, we can also go beyond the LDA and describe the atoms using discrete energies and exact eigenfunctions to estimate response functions [27]. The predictions are shown with the dashed line in Fig. 2b-d, deviating from the LDA for the tightest confinements, likely due to the trap frequency approaching the recoil. Lastly, normalizing the measured susceptibility by the Fermi energy provides a measurement of the trap-averaged Lindhard function as a function of the dimensionless momentum, showing a monotonic response at all momenta and the absence of Fermi nesting, as can be seen in Fig. 2d.

We now leverage our mesoscopic preparation procedure to track superradiance as a function of atom number. We fix $\tilde{\Delta}_p = 2\pi \times 1.3$ MHz corrected for the atom-number dependent dispersive shift, and acquire photon traces with varying atom numbers between $N = 70$ and 2100 and trap frequencies, to span a wide range of k_{\pm}/k_F . To further eliminate spurious atom-number dependent biases, the magnetic field is ramped to 566 G reducing the atom-atom scattering length to zero. The results are shown in Fig. 3a, together with the threshold inferred from the increase of photon number in the corresponding traces. The thresholds observed over the whole range of parameters are in reasonable agreement with the zero-temperature LDA theory. Similar to the density-dependence investigations in Fig. 2, the variation of atom number also tracks the susceptibility as a function of k_{\pm}/k_F . The results, normalized by atom number, are presented in Fig. 3b, together with the theoretical predictions.

A distinctive feature of the superradiant phase is the super-linear scaling of the light intensity with atom number, due to the constructive interference of the light scattered by each of the atoms [23, 35]. Figure 3c shows the photon number observed in the superradiant phase as a function of atom number, for a fixed value of the pump strength V_0 , matching well the power law $N_{\text{ph}} \propto N^2$ expected for classical particles. This behavior persists as the integration time is varied [27]. Correction to the superradiant scaling of the photon number with k/k_F , resulting from Pauli-blocking effects, are expected to be small in our parameter regime [27].

Our Fermi gas comprises an equal mixture of two hyperfine states, separated by a frequency $\Delta_{\text{HFS}}/2\pi = 165$ MHz. So far, we have operated in a regime where the cavity field is red-detuned from both states, such that the photons exert forces of the same sign on both spin components. Consequently, the resulting superradiant phase has a charge density wave character. Our mesoscopic Fermi gas also allows to operate

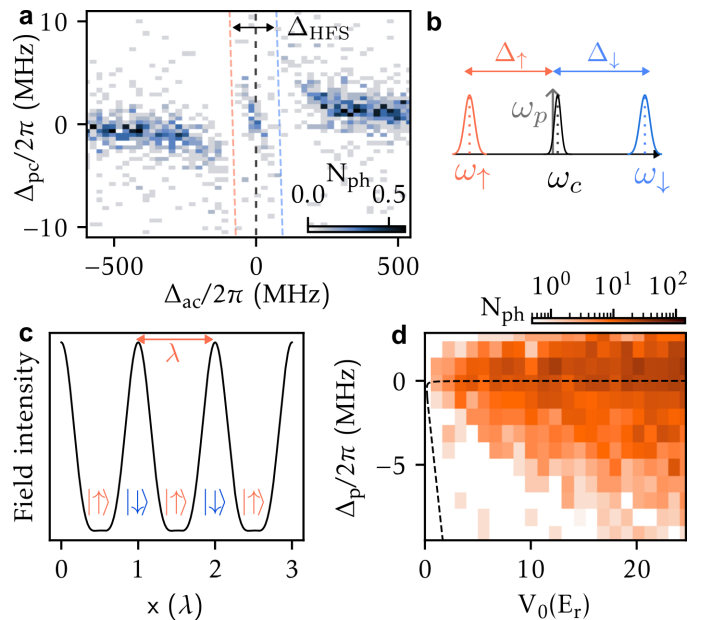


FIG. 4. Magnetic superradiance (a) Cavity transmission spectrum showing two avoided crossings corresponding to the cavity being on resonance with states $|\uparrow\rangle$ (--) and $|\downarrow\rangle$ (--) respectively. Δ_{pc} refers to the detuning between the cavity probe and the cavity resonance and Δ_{ac} is the detuning between the atomic resonances and the cavity resonance. Each vertical line is averaged 15 times. To study magnetic superradiance, we fix the cavity resonance in between the two states (--) as shown in (b). (c) Sketch of the light intensity produced by the combined pump and cavity fields in the superradiant phase along the cavity direction, repulsive for $|\uparrow\rangle$ and attractive for $|\downarrow\rangle$, trapping atoms at node and antinodes respectively. (d) Photon numbers detected as a function of Δ_p and V_0 showing superradiance in the magnetic regime for $N = 520 \pm 40$ atoms and the LDA prediction for the threshold (--). Each data point is averaged between 2 and 4 times.

in the regime where the forces are opposite for the two spin components, by tuning the cavity resonance frequency halfway between the two hyperfine levels as shown in Fig. 4a and b. There, the existence of a dispersive regime requires the collective Rabi splitting to be lower than half the energy splitting between states, forcing $N \ll (\Delta_{\text{HFS}}/4g)^2 = 3400$. The opposite potentials exerted by light on the two spin components, or equivalently their opposite refractive index, implies that the organized phase has a spin-density wave character [27]: the interference pattern between the pump field and cavity field localizes spin $|\uparrow\rangle$ atoms at minima and spin $|\downarrow\rangle$ at maxima of the field intensity, as illustrated in Figure 4c. This situation differs from magnetic structures produced with two spin components coherently coupled by Raman transitions involving cavity photons [36–38]. In our case, the negligible hyperfine mixing of the excited state of the transition suppresses Raman couplings, and the ordered phase can only feature Ising-type longitudinal spin structures without transverse component.

Figure 4a presents the transmission spectrum of the cavity containing a total of $N = 520 \pm 40$ atoms, as its resonance is scanned through the two hyperfine states. We observe a clear

transmission window between the two hyperfine resonances where the dispersive shift is zero. In this configuration, we repeat the protocol described above and observe the onset of the superradiant phase. The results are presented in Figure 4d. Generalizing the stability analysis [32] to opposite spin coupling yields a phase boundary determined by the spin susceptibility of the system at the relevant wavevectors [27]. In contrast with density-wave ordering at similar atom number, here we find strong deviations from the theory. It is known that the linear stability analysis does not capture well the phase boundary for light producing a repulsive potential [39], where superradiance only exists within a narrow detuning range around the cavity resonance, and we suspect similar effects here. However, the phase diagram in Fig. 4d is qualitatively similar to that of red-detuned cavities, calling for a finer theoretical understanding of this new regime.

To confirm qualitatively the magnetic nature of the ordering, we repeated the experiment at two different magnetic fields, 316 and 566 G, thereby changing the scattering length characterizing the contact interactions from $a = -890 a_0$ to 0 [30]. Mapping out the observed phase boundary onto a susceptibility using the same procedure as above yields a reduction by about 35% by attractive interactions. Indeed, magnetic ordering is expected to compete with attractive interactions, a feature well known for example in Fermi liquids [1].

In conclusion, we have explored cavity-induced superradiance in a mesoscopic Fermi gas, charting its interplay with Fermi statistics. Our results reveal a non-monotonic threshold when compressing the gas at fixed atom number, due to the Fermi-pressure-induced occupation of finite momentum states at zero temperature.

Interestingly, our findings are reminiscent of the interplay of between temperature-induced momentum occupation and recoil processes predicted to yield a temperature-enhanced superradiance in Bose gases [34], a feature so far never observed experimentally. Operating in the mesoscopic quantum gas regime has important implications for future quantum simulations: for any cavity QED experiment in the optical regime, producing an entangled state of N atoms using cavity-mediated interactions requires a cooperativity $O(N^2)$ down to $O(N)$ for heralded protocols [40]. Our mesoscopic Fermi gas opens the possibility to reach a break-even point where system-wide entanglement mediated by light could emerge in cavities with realistic cooperativities from few tens to hundreds [41–43]. Apart from the creation of entanglement, the mesoscopic regime will make it possible to study genuinely quantum effects beyond mean-field in self-organization [44]. In addition, mesoscopic samples may allow for increasing the number of available cavity modes [45, 46] beyond the number of particles, a prerequisite for the realisation of some quantum chaotic models [47–50]. Lastly, our platform can also be scaled by projecting several tweezer traps, loaded from a single reservoir in order to investigate tunnel-coupled gases [51–53] in the presence of strong light-matter interactions, generalizing to quantum matter the pioneering work performed with thermal atoms [18].

Acknowledgments — We thank Alexander Baumgärtner for discussions, Michał Zdziennicki, Tabea Bühler, Francesco Piazza, Michele Pini and Tobias Donner for careful reading of the manuscript and discussions. We acknowledge funding from the Swiss State Secretariat for Education, Research and Innovation (Grants No. MB22.00063 and 20QU-1.215924) and the Swiss National Science Foundation (Grant No. 217124).

-
- [1] D. Pines and P. Nozières, *The Theory of Quantum Liquids*, Vol. 1 (Addison-Wesley, California, 1989).
 - [2] T. Busch, J. R. Anglin, J. I. Cirac, and P. Zoller, Inhibition of spontaneous emission in fermi gases, *Europhysics Letters* **44**, 1 (1998).
 - [3] B. Shuve and J. H. Thywissen, Enhanced pauli blocking of light scattering in a trapped fermi gas, *Journal of Physics B: Atomic, Molecular and Optical Physics* **43**, 015301 (2009).
 - [4] A. Görlitz, A. P. Chikkatur, and W. Ketterle, Enhancement and suppression of spontaneous emission and light scattering by quantum degeneracy, *Phys. Rev. A* **63**, 041601 (2001).
 - [5] Y. Margalit, Y.-K. Lu, F. Çağrı Top, and W. Ketterle, Pauli blocking of light scattering in degenerate fermions, *Science* **374**, 976 (2021).
 - [6] C. Sanner, L. Sonderhouse, R. B. Hutson, L. Yan, W. R. Milner, and J. Ye, Pauli blocking of atom-light scattering, *Science* **374**, 979 (2021).
 - [7] R. Jannin, Y. van der Werf, K. Steinebach, H. L. Bethlem, and K. S. E. Eikema, Pauli blocking of stimulated emission in a degenerate fermi gas, *Nature Communications* **13** (2022).
 - [8] A. B. Deb and N. Kjærgaard, Observation of pauli blocking in light scattering from quantum degenerate fermions, *Science* **374**, 972 (2021).
 - [9] H. Tanji-Suzuki, I. D. Leroux, M. H. Schleier-Smith, M. Cetina, A. T. Grier, J. Simon, and V. Vuletić, Chapter 4 - interaction between atomic ensembles and optical resonators: Classical description, in *Advances in Atomic, Molecular, and Optical Physics*, Vol. 60, edited by E. Arimondo, P. Berman, and C. Lin (Academic Press, 2011) pp. 201–237.
 - [10] S. Haroche, Nobel lecture: Controlling photons in a box and exploring the quantum to classical boundary, *Rev. Mod. Phys.* **85**, 1083 (2013).
 - [11] A. Reiserer and G. Rempe, Cavity-based quantum networks with single atoms and optical photons, *Rev. Mod. Phys.* **87**, 1379 (2015).
 - [12] A. T. Black, H. W. Chan, and V. Vuletić, Observation of collective friction forces due to spatial self-organization of atoms: From rayleigh to bragg scattering, *Phys. Rev. Lett.* **91**, 203001 (2003).
 - [13] K. Baumann, C. Guerlin, F. Brennecke, and T. Esslinger, Dicke quantum phase transition with a superfluid gas in an optical cavity, *Nature* **464**, 1301–1306 (2010).
 - [14] J. Klinder, H. Keßler, M. Wolke, L. Mathey, and A. Hemmerich, Dynamical phase transition in the open dicke model, *Proceedings of the National Academy of Sciences* **112**, 3290–3295 (2015).

- [15] A. J. Kollár, A. T. Papageorge, V. D. Vaidya, Y. Guo, J. Keeling, and B. L. Lev, Supermode-density-wave-polariton condensation with a bose–einstein condensate in a multimode cavity, *Nature Communications* **8** (2017).
- [16] X. Zhang, Y. Chen, Z. Wu, J. Wang, J. Fan, S. Deng, and H. Wu, Observation of a superradiant quantum phase transition in an intracavity degenerate fermi gas, *Science* **373**, 1359 (2021).
- [17] V. Helson, T. Zewtler, F. Mivehvar, E. Colella, K. Roux, H. Konishi, H. Ritsch, and J.-P. Brantut, Density-wave ordering in a unitary fermi gas with photon-mediated interactions, *Nature* **618**, 716–720 (2023).
- [18] J. Ho, Y.-H. Lu, T. Xiang, C. C. Rusconi, S. J. Masson, A. Asenjo-Garcia, Z. Yan, and D. M. Stamper-Kurn, Optomechanical self-organization in a mesoscopic atom array, *Nature Physics* **21**, 1071–1077 (2025).
- [19] J. Keeling, M. J. Bhaseen, and B. D. Simons, Fermionic superradiance in a transversely pumped optical cavity, *Phys. Rev. Lett.* **112**, 143002 (2014).
- [20] F. Piazza and P. Strack, Umklapp superradiance with a collisionless quantum degenerate fermi gas, *Phys. Rev. Lett.* **112**, 143003 (2014).
- [21] Y. Chen, Z. Yu, and H. Zhai, Superradiance of degenerate fermi gases in a cavity, *Physical Review Letters* **112** (2014).
- [22] D. Ortuño-Gonzalez, R. Lin, J. Stefaniak, A. Baumgärtner, G. Natale, T. Donner, and R. Chitra, Pauli crystal superradiance, [arXiv:2505.02837](https://arxiv.org/abs/2505.02837) (2025).
- [23] Z. Yan, J. Ho, Y.-H. Lu, S. J. Masson, A. Asenjo-Garcia, and D. M. Stamper-Kurn, Superradiant and subradiant cavity scattering by atom arrays, *Phys. Rev. Lett.* **131**, 253603 (2023).
- [24] R. M. Sandner, W. Niedenzu, F. Piazza, and H. Ritsch, Self-ordered stationary states of driven quantum degenerate gases in optical resonators, *Europhysics Letters* **111**, 53001 (2015).
- [25] F. Mivehvar, H. Ritsch, and F. Piazza, Superradiant topological peierls insulator inside an optical cavity, *Physical Review Letters* **118** (2017).
- [26] F. Orsi, N. Sauerwein, R. P. Bhatt, J. Faltinath, E. Fedotova, N. Reiter, T. Cantat-Moltrecht, and J.-P. Brantut, Cavity microscope for micrometer-scale control of atom-photon interactions, *PRX Quantum* **5** (2024).
- [27] See Supplemental Material at [URL] for details on the experimental procedures, theoretical descriptions and supplementary data, which includes Refs. [54–65].
- [28] D. M. Stamper-Kurn, H.-J. Miesner, A. P. Chikkatur, S. Inouye, J. Stenger, and W. Ketterle, Reversible formation of a bose–einstein condensate, *Phys. Rev. Lett.* **81**, 2194 (1998).
- [29] F. Serwane, G. Zürn, T. Lompe, T. B. Ottenstein, A. N. Wenz, and S. Jochim, Deterministic preparation of a tunable few-fermion system, *Science* **332**, 336 (2011).
- [30] G. Zürn, T. Lompe, A. N. Wenz, S. Jochim, P. S. Julienne, and J. M. Hutson, Precise characterization of ^6Li feshbach resonances using trap-sideband-resolved rf spectroscopy of weakly bound molecules, *Phys. Rev. Lett.* **110**, 135301 (2013).
- [31] T. Zewtler, G. Del Pace, F. Marijanovic, S. Chattopadhyay, T. Bühler, C.-M. Halati, L. Skolc, L. Tolle, V. Helson, G. Bolognini, A. Fabre, S. Uchino, T. Giamarchi, E. Demler, and J. P. Brantut, Nonequilibrium dynamics of long-range interacting fermions, *Phys. Rev. X* **15**, 021089 (2025).
- [32] F. Marijanović, S. Chattopadhyay, L. Skolc, T. Zewtler, C.-M. Halati, S. B. Jäger, T. Giamarchi, J.-P. Brantut, and E. Demler, Dynamical instabilities of strongly interacting ultracold fermions in an optical cavity, [arXiv:2406.13548](https://arxiv.org/abs/2406.13548) (2024).
- [33] J. Lindhard, On the properties of a gas of charged particles, *Kgl. Danske Videnskab. Selskab Mat.-fys. Medd.* **Vol: 28, No. 8** (1953).
- [34] F. Piazza, P. Strack, and W. Zwerger, Bose–einstein condensation versus dicke–hepp–lieb transition in an optical cavity, *Annals of Physics* **339**, 135 (2013).
- [35] P. Domokos and H. Ritsch, Collective cooling and self-organization of atoms in a cavity, *Phys. Rev. Lett.* **89**, 253003 (2002).
- [36] Z. Zhiqiang, C. H. Lee, R. Kumar, K. J. Arnold, S. J. Masson, A. S. Parkins, and M. D. Barrett, Nonequilibrium phase transition in a spin-1 dicke model, *Optica* **4**, 424 (2017).
- [37] R. M. Kroeze, Y. Guo, V. D. Vaidya, J. Keeling, and B. L. Lev, Spinor self-ordering of a quantum gas in a cavity, *Physical Review Letters* **121**, 163601 (2018).
- [38] M. Landini, N. Dogra, K. Kroeger, L. Hruby, T. Donner, and T. Esslinger, Formation of a spin texture in a quantum gas coupled to a cavity, *Phys. Rev. Lett.* **120**, 223602 (2018).
- [39] P. Zupancic, D. Dreon, X. Li, A. Baumgärtner, A. Morales, W. Zheng, N. R. Cooper, T. Esslinger, and T. Donner, p -band induced self-organization and dynamics with repulsively driven ultracold atoms in an optical cavity, *Phys. Rev. Lett.* **123**, 233601 (2019).
- [40] A. S. Sørensen and K. Mølmer, Measurement induced entanglement and quantum computation with atoms in optical cavities, *Phys. Rev. Lett.* **91**, 097905 (2003).
- [41] S. Jandura, V. Srivastava, L. Pecorari, G. K. Brennen, and G. Pupillo, Nonlocal multiqubit quantum gates via a driven cavity, *Phys. Rev. A* **110**, 062610 (2024).
- [42] B. Grinkemeyer, E. Guardado-Sanchez, I. Dimitrova, D. Shchepanovich, G. E. Mandopoulou, J. Borregaard, V. Vuletić, and M. D. Lukin, Error-detected quantum operations with neutral atoms mediated by an optical cavity, *Science* **387**, 1301 (2025).
- [43] G. S. Bolognini, Z. Xue, M. A. Eichenberger, N. Sauerwein, F. Orsi, E. Fedotova, R. P. Bhatt, and J. P. Brantut, Design and assembly of a cavity microscope with high numerical aperture for quantum simulations, *Opt. Express* **33**, 44051 (2025).
- [44] K. Müller and W. T. Strunz, Genuine quantum effects in dicke-type models at large atom numbers, *Phys. Rev. Lett.* **135**, 123602 (2025).
- [45] V. D. Vaidya, Y. Guo, R. M. Kroeze, K. E. Ballantine, A. J. Kollár, J. Keeling, and B. L. Lev, Tunable-range, photon-mediated atomic interactions in multimode cavity qed, *Phys. Rev. X* **8**, 011002 (2018).
- [46] R. M. Kroeze, B. P. Marsh, D. A. Schuller, H. S. Hunt, A. N. Bourzutschky, M. Winer, S. Gopalakrishnan, J. Keeling, and B. L. Lev, Directly observing replica symmetry breaking in a vector quantum-optical spin glass, *Science* **389**, 1122 (2025).
- [47] P. Urich, S. Bandyopadhyay, N. Sauerwein, J. Sonner, J.-P. Brantut, and P. Hauke, A cavity quantum electrodynamics implementation of the sachdev–ye–kitaev model, [arXiv:2303.11343](https://arxiv.org/abs/2303.11343) (2023).
- [48] R. Baumgartner, P. Pelliconi, S. Bandyopadhyay, F. Orsi, N. Sauerwein, P. Hauke, J.-P. Brantut, and J. Sonner, Quantum simulation of the sachdev–ye–kitaev model using time-dependent disorder in optical cavities, [arXiv:2411.17802](https://arxiv.org/abs/2411.17802) (2024).
- [49] D. Pascual Solis, A. Windey, S. Bandyopadhyay, A. Legramandi, and P. Hauke, From single-particle to many-body chaos in yukawa–syk: theory and a cavity-qed proposal, [arXiv:2511.04762](https://arxiv.org/abs/2511.04762) (2025).
- [50] R. L. Baumgartner, P. Pelliconi, S. Bandyopadhyay, F. Orsi, P. Hauke, J.-P. Brantut, and J. Sonner, Quantum simulation using trotterized disorder hamiltonians in a single-mode optical cavity, [arXiv:2512.13774](https://arxiv.org/abs/2512.13774) (2025).

- [51] S. Murmann, A. Bergschneider, V. M. Klinkhamer, G. Zürn, T. Lompe, and S. Jochim, Two fermions in a double well: Exploring a fundamental building block of the hubbard model, [Phys. Rev. Lett. **114**, 080402 \(2015\)](#).
- [52] B. M. Spar, E. Guardado-Sanchez, S. Chi, Z. Z. Yan, and W. S. Bakr, Realization of a fermi-hubbard optical tweezer array, [Phys. Rev. Lett. **128**, 223202 \(2022\)](#).
- [53] N. Jain, J. Zhang, M. Culemann, and P. M. Preiss, Programmable assembly of ground state fermionic tweezer arrays, [arXiv:2512.09849 \(2025\)](#).
- [54] N. Sauerwein, F. Orsi, P. Urich, S. Bandyopadhyay, F. Mattiotti, T. Cantat-Moltrecht, G. Pupillo, P. Hauke, and J.-P. Brantut, Engineering random spin models with atoms in a high-finesse cavity, [Nature Physics **19**, 1128–1134 \(2023\)](#).
- [55] M. Endo and T. R. Schibli, Residual phase noise suppression for pound-drever-hall cavity stabilization with an electro-optic modulator, [OSA Continuum **1**, 116 \(2018\)](#).
- [56] P. Vezio, G. Vinelli, C. Mancini, L. Chao, G. Rosi, G. M. Tino, and L. Salvi, Enhanced laser frequency stabilization to a high-finesse cavity through a combined feed-back and feed-forward correction, [Opt. Express **33**, 36163 \(2025\)](#).
- [57] S. K. Lee, J. J. Kim, and D. Cho, Transformable optical dipole trap using a phase-modulated standing wave, [Phys. Rev. A **74**, 063401 \(2006\)](#).
- [58] K. C. Cox, G. P. Greve, B. Wu, and J. K. Thompson, Spatially homogeneous entanglement for matter-wave interferometry created with time-averaged measurements, [Phys. Rev. A **94**, 061601 \(2016\)](#).
- [59] M. H. Seo, S. Park, and D. Cho, Relaxation of atomic temperature anisotropy in a one-dimensional optical lattice enhanced by dynamic control of the aspect ratio, [Phys. Rev. A **101**, 043611 \(2020\)](#).
- [60] K. Roux, V. Helson, H. Konishi, and J. P. Brantut, Cavity-assisted preparation and detection of a unitary fermi gas, [New Journal of Physics **23**, 043029 \(2021\)](#).
- [61] D. Shadmany, A. Kumar, A. Soper, L. Palm, C. Yin, H. Ando, B. Li, L. Taneja, M. Jaffe, D. Schuster, and J. Simon, Cavity qed in a high na resonator, [Science Advances **11** \(2025\)](#).
- [62] T. N. C. Bühler, T. Zwettler, G. S. Bolognini, A. H. Fabre, V. Y. Helson, G. D. Pace, and J.-P. Brantut, Direct production of fermionic superfluids in a cavity-enhanced optical dipole trap, [SciPost Phys. **18**, 133 \(2025\)](#).
- [63] R. Kubo, Statistical-mechanical theory of irreversible processes. i. general theory and simple applications to magnetic and conduction problems, [Journal of the Physical Society of Japan **12**, 570 \(1957\)](#).
- [64] B. Mihaila, Lindhard function of a d-dimensional fermi gas, [arXiv:1111.5337 \(2011\)](#).
- [65] S. Chen and Y. Chen, Detecting the fermi surface nesting effect for the fermionic dicke transition by trap-induced localization, [Phys. Rev. A **110**, 013312 \(2024\)](#).

SUPPLEMENTAL MATERIAL

A. Experimental apparatus

The core of the experimental apparatus is the cavity-microscope device described in [26, 54]. The optical cavity has a finesse of 5265 at 671 nm, near-resonant to the D2 transition of ${}^6\text{Li}$, and a finesse of 19 306 at 1342 nm. The latter wavelength is used both to stabilize the cavity length and to generate a deep intracavity dipole trap. The cavity length is 25.987 mm, corresponding to a free spectral range of $\nu_{\text{FSR}} = 5.77$ GHz, and it is operated approximately 100 μm from concentric. At 671 nm, this results in a cavity linewidth of $\kappa/2\pi = 1.1$ MHz and a maximum single-atom single-photon coupling $g/2\pi = 2$ MHz at 671 nm, corresponding to a cooperativity $\eta = 4g^2/\kappa\Gamma = 2.52$.

The lenses in the mirror-lens assemblies have a numerical aperture of 0.345. The lenses are optimized to be aberration-free at 780 nm. From parametric heating, we measure a transverse to longitudinal trap frequency ratio of 5.5, from which we infer a tweezer waist of 0.95 μm , close to the diffraction limit of 0.8 μm , and a Rayleigh range of 3.68 μm . The wavelength of the tweezer beam is monitored with a wavemeter and set to 765 nm where we found transmission through the cavity mirrors to be maximum.

We operate the experiment with a single laser at 1342 nm, whose frequency is stabilized with a Pound-Drever-Hall (PDH) lock on the cavity resonance. The PDH light acts at the same time as the intra-cavity dipole trap. Additional noise reduction of the intracavity dipole trap is achieved by fast feedback of the PDH error signal onto an electro-optic modulator, following methods similar to [55, 56]. The same modulator is also used to generate sidebands for canceling the intracavity lattice [57–62]. During evaporative cooling, the intracavity field is reduced using an acousto-optic modulator, and we compensate the reduction of PDH signal using a separate modulator acting before the photodiode. Liquid-crystal attenuators placed in front of the photodiodes increase the available range of power for which we can lock the cavity.

The 1342 nm laser is frequency doubled to 671 nm using a second-harmonic-generation cavity (Toptica TA-SHG). This light is used for Zeeman slowing, magneto-optical trapping, absorption imaging, cavity probing, and transverse pumping. Control of the atom-cavity detuning is achieved using a beat-note lock to another laser stabilized onto lithium using saturated absorption spectroscopy, with feedback onto the cavity length.

B. Experimental sequence

The experimental sequence begins by loading a magneto-optical trap of ${}^6\text{Li}$ atoms for 1.5 seconds near the center of the cavity, using light near resonant with the D2 transition. The magnetic compensation coils are then adjusted to overlap the atomic cloud with the cavity mode center in the presence of both the intracavity dipole trap and the optical tweezer, with respective trap depths of about 1240 and 10 μK . To

maximize loading efficiency, the lattice structure formed by the intracavity dipole trap is canceled by phase-modulating the incident at a frequency equal to the free spectral range. The magneto-optical trap is subsequently compressed over 16 ms by simultaneously reducing laser powers, magnetic field gradients, and detunings. After switching off the cooling light and magnetic fields, approximately one million atoms remain trapped at the cavity center in a mixture of the two lowest hyperfine states $|1\rangle, |2\rangle = |{}^2S_{F=1/2}, m_F = \pm 1/2\rangle$.

The magnetic field is ramped to 316 G, and atoms are transferred from state $|2\rangle$ to state $|3\rangle = |{}^2S_{F=3/2}, m_F = -3/2\rangle$ using a radiofrequency Landau-Zener sweep from 85 to 90 MHz over 1 ms, with an efficiency of 85%. At this field, the scattering length between states $|1\rangle$ and $|3\rangle$ is $a = -890.5a_0$ [30]. In the main text, we refer to the hyperfine states as $|1\rangle = |\downarrow\rangle$ and $|3\rangle = |\uparrow\rangle$. Evaporative cooling is then performed using four piecewise linear ramps of the intracavity trap power over a total duration of 500 ms resulting in approximately 30000 atoms at a temperature of 400 nK. This corresponds to a $T/T_F = 1.14$ for atoms in the cavity dipole trap, which has a final trap depth of 1.38 μK , and to 0.01 at the bottom of the tweezer trap. We measure an upper bound for the temperature of the atoms in the cavity dipole trap with standard time-of-flight technique, and we assume that the atoms are in thermal equilibrium. After switching-off the intracavity dipole trap, we obtain a degenerate Fermi gas of approximately 4000 atoms trapped in a tweezer at the center of the cavity mode, in a balanced spin mixture. For measurements in the non-interacting regime, the magnetic field is ramped to 566 G over 200 ms prior to illumination with the transverse pump laser, while for interacting measurements it is held constant. The tweezer power is adjusted to vary the atom number and subsequently increased to reach the desired Fermi wavevector, varying the transverse trap frequency between 5 and 90 kHz.

To trigger the superradiant phase transition, the power of the transverse side pump is quenched from zero to its target value within 4 μs . Photons leaking from the cavity are detected using a single-photon counting module. The side pump is detuned from both the empty cavity resonance and the atomic resonance of state $|\uparrow\rangle$, and has a waist of 89 μm , measured by direct imaging in the atomic plane. After all measurements are performed, all traps are released and the empty cavity resonance is measured using on-axis transmission spectroscopy.

C. Data processing

1. Extraction of the threshold

We determine the critical pump power by recording the total number of detected photons leaking from the cavity over the first 30 μs following the quench. We found that increasing this duration improves the signal to noise ratio at the expense of a visible decay in photon population, likely originating from atom losses in the superradiant state, while reducing it reduces the signal below the noise floor.

Because of the small atom number and limited photon collection efficiency, the total photon count recorded per run of the experiment is low and subject to significant noise, primarily photon shot noise and shot-to-shot atom number fluctuations. To mitigate these effects on the threshold determination, we use a Gaussian filter on the photon count data to average neighboring values of V_0 . We then determine the pump power at which the signal exceeds a critical photon number. The robustness of this procedure is verified by varying the critical photon number by $\pm 30\%$ and tracking the resulting critical pump power. The error bars shown correspond to the mean and standard deviation of the critical values obtained over this range. If the standard deviation is zero, we instead use the bin width to represent the uncertainty.

For measurements of Figure 3c where the atom and photon number varies by more than one order of magnitude, the threshold value is adjusted accordingly. We verify that the extracted critical pump strength remains robust against variations in both the threshold choice and the signal integration time.

2. Uncertainty on atom numbers

Atom numbers are measured using absorption imaging after a $60\mu\text{s}$ time of flight and with a pulse duration of $10\mu\text{s}$. The imaging is calibrated against the dispersive shift of the cavity resonance at high atom numbers. The dispersive shift measurement fails at low atom number where it becomes smaller than the cavity linewidth. Thus for the data shown in Figure 3c, atom numbers are averaged between absorption imaging and dispersive shift measurements. For Figures 2, 4 and S1 only absorption imaging is used.

For low atom numbers, we estimate the uncertainty in atom numbers using a bootstrapping procedure on the absorption images. We believe that the stated uncertainty for low atom numbers is dominated by detection noise rather than sample preparation, due to the relatively good stability of the superradiance data. The resulting standard deviation of the mean is compared to that obtained from single-image measurements in a higher atom number regime, where reliable atom counting from individual images is possible. This analysis shows excellent agreement between the mean atom numbers extracted using both methods, as well as good agreement in the estimated uncertainties.

3. Atom number dependence

Figure 3a shows the onset of superradiance with different atom numbers, at a fixed detuning of the pump from the dispersively shifted cavity resonance $\tilde{\Delta}_p$. For all atom numbers, we observe the superradiant transition in the V_0 – Δ_p plane, as shown in two examples in Fig. S1a-c for $N = 1120 \pm 120$, $N = 320 \pm 48$ and 108 ± 60 , respectively. There, we fix $\Delta_\uparrow = 2\pi \times 414\text{MHz}$. For the largest number of atoms, the cavity resonance, i.e. the tip of the corner-shaped pattern in Fig. S1a-b is significantly shifted. While for Figure 2

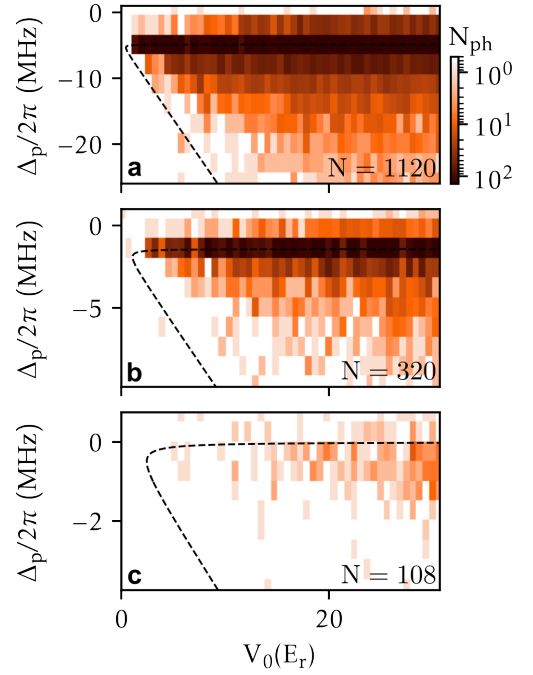


FIG. S1. (a-c) Photon number recorded within $30\mu\text{s}$ following a quench as a function of both V_0 and Δ_p plane for (a) $N = 1120 \pm 120$, (b) $N = 320 \pm 48$ and (c) $N = 108 \pm 60$. The dashed line (--) represents the LDA predictions for the thresholds. Measurements are taken at $\Delta_\uparrow/2\pi = 414\text{MHz}$. Each data is averaged 2 times. Both measurements are taken at the same tweezer trap depth of $11\mu\text{K}$, resulting in $k/k_F = (0.63, 0.75, 0.9)$ for the three atom numbers.

the detuning was kept constant and chosen to minimize the threshold, for the data of Figure 3 the detuning was measured and adapted for each atom number.

4. Photon number scaling

Figure S2 shows the photon number collected by the single-photon counter after the onset of superradiance, plotted as a function of atom number for different collection times. Increasing the collection time shifts the absolute photon count but does not affect the scaling, confirming the observed atom-number dependence.

D. Theoretical model

1. Critical point

To describe the onset of cavity superradiance following a quench of the transverse pump, we apply the linear-response treatment developed in [31, 32]. For the moment we treat the gas as spinless. We start from the cavity-QED Hamiltonian in the dispersive regime,

$$\hat{H} = \tilde{\Delta}_p \hat{a}^\dagger \hat{a} - \frac{g\Omega}{2\Delta} \hat{\theta}(\hat{a} + \hat{a}^\dagger) \quad (\text{S2})$$

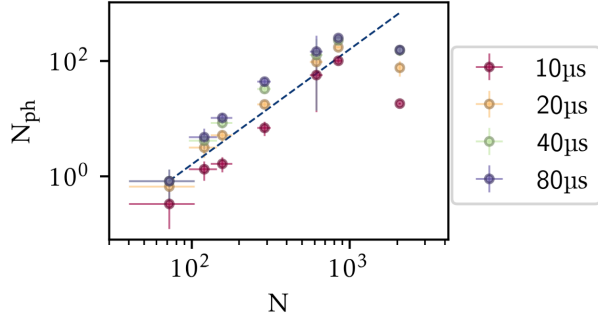


FIG. S2. Photon number scaling from Figure 3c for different collection times after the quench. Increasing the collection time changes the offset of the signal but does not affect the scaling with atom number. Error bars on the photon number represent the standard deviation of the mean, calculated from different experimental repetitions.

where $\tilde{\Delta}_p$ is the detuning of the pump from the dispersively shifted cavity resonance and \hat{a}^\dagger, \hat{a} the raising and lowering operators for the cavity field. g is the single-atom single-photon coupling strength of the atomic transition to the cavity field and Ω the Rabi frequency of the pump. Δ is the pump detuning from the atomic transition. The density-wave operator

$$\hat{\theta} = \int d\mathbf{r} \hat{n}(\mathbf{r}) \cos(\mathbf{k}_c \cdot \mathbf{r}) \cos(\mathbf{k}_p \cdot \mathbf{r}) \quad (\text{S3})$$

captures the coupling between the atomic density modulation and the interference of the pump with the cavity field. Here, $\hat{n}(\mathbf{r})$ is the fermionic density operator, defined as

$$\hat{n}(\mathbf{r}) = \hat{\psi}_g^\dagger(\mathbf{r})\hat{\psi}_g(\mathbf{r}) = \sum_{ij} \phi_i^*(\mathbf{r})\phi_j(\mathbf{r})\hat{c}_i^\dagger\hat{c}_j, \quad (\text{S4})$$

where $\hat{\psi}_g(\mathbf{r})$ is the field operator for atoms in the ground state, \hat{c}_i (\hat{c}_i^\dagger) are the corresponding annihilation (creation) operators satisfying the fermionic anticommutation relations $\{\hat{c}_i, \hat{c}_j^\dagger\} = \delta_{ij}$ with δ_{ij} the Kronecker delta, and $\phi_i(\mathbf{r})$ are the single-particle eigenfunctions of the unperturbed system. This eigenbasis will be used in Section E to calculate the density-density response function.

Introducing the cavity field quadratures

$$\begin{cases} \hat{X} = \frac{1}{\sqrt{2}}(\hat{a} + \hat{a}^\dagger) \\ \hat{P} = \frac{1}{\sqrt{2}i}(\hat{a} - \hat{a}^\dagger) \end{cases} \quad (\text{S5})$$

the Hamiltonian becomes

$$\hat{H} = \frac{\tilde{\Delta}_p}{2}(\hat{X}^2 + \hat{P}^2) - \frac{\sqrt{2}g\Omega}{2\Delta}\hat{\theta}\hat{X} \quad (\text{S6})$$

The early-time dynamics after the quench is described by the Heisenberg-Langevin equations for the cavity field, combined with linear response for the atomic degrees of

freedom described by the Kubo formalism [63]. This yields the coupled equations for the expectation values

$$\begin{cases} \frac{d\langle\hat{X}\rangle}{dt} = \tilde{\Delta}_p\langle\hat{P}\rangle - \frac{\kappa}{2}\langle\hat{X}\rangle \\ \frac{d\langle\hat{P}\rangle}{dt} = -\tilde{\Delta}_p\langle\hat{X}\rangle - \frac{\kappa}{2}\langle\hat{P}\rangle + \frac{\sqrt{2}g\Omega}{2\Delta}\langle\hat{\theta}(t)\rangle \\ \langle\hat{\theta}(t)\rangle = \frac{\sqrt{2}g\Omega}{2\Delta} \int_0^\infty \chi(t-t')\langle\hat{X}(t')\rangle dt' \end{cases} \quad (\text{S7})$$

where we used $\langle\hat{\theta}(t=0)\rangle = 0$ in the absence of pumping. We define χ as the density-wave susceptibility of a single spin component

$$\chi(t-t') = -i\Upsilon(t-t')\langle[\hat{\theta}(t), \hat{\theta}(t')]\rangle, \quad (\text{S8})$$

with $\Upsilon(t)$ the Heaviside step function.

Going to Fourier space and considering the onset of an unstable solution to Equations S7 yields the threshold condition in terms of the zero-frequency susceptibility:

$$\chi(\omega \rightarrow 0) = \frac{\tilde{\Delta}_p^2 + (\kappa/2)^2}{\tilde{\Delta}_p} \frac{2\Delta^2}{g^2\Omega^2} \quad (\text{S9})$$

$$= \frac{1}{2D_{0c}}. \quad (\text{S10})$$

For simplicity, we will denote this quantity simply as χ in the following. We have introduced an effective cavity-induced non-linearity

$$D_{0c} = \frac{\tilde{\Delta}_p V_{0c} U_0}{\tilde{\Delta}_p^2 + (\kappa/2)^2}, \quad (\text{S11})$$

where $V_{0c} = \Omega_c^2/4\Delta$ the critical pump-induced lattice depth and $U_0 = g^2/\Delta$ the dispersive shift per cavity photon.

2. Two-component gas

We now generalize the above treatment to a two-component Fermi gas with potentially unequal light-matter coupling strengths. Each spin component contributes with its own density-wave susceptibility χ , while the cavity couples to a collective density modulation involving both components. Introducing density-wave operators $\hat{\theta}_i$ for each spin component $i = \uparrow, \downarrow$, the Hamiltonian becomes

$$\hat{H} = \tilde{\Delta}_p \hat{a}^\dagger \hat{a} - \frac{g_\uparrow \Omega_\uparrow}{2\Delta_\uparrow} (\hat{\theta}_\uparrow + \zeta \hat{\theta}_\downarrow) (\hat{a} + \hat{a}^\dagger), \quad (\text{S12})$$

expressed as a function of the dimensionless asymmetry parameter

$$\zeta = \frac{\Delta_\uparrow g_\downarrow \Omega_\downarrow}{\Delta_\downarrow g_\uparrow \Omega_\uparrow}. \quad (\text{S13})$$

We introduce the collective operator $\hat{\Theta} = \hat{\theta}_\uparrow + \zeta \hat{\theta}_\downarrow$, which couples linearly to the cavity field. The cavity therefore

probes an effective collective susceptibility, which we denote by χ_{eff} , defined as

$$\chi_{\text{eff}}(t-t') = -i\Upsilon(t-t')\langle[\hat{\Theta}(t), \hat{\Theta}(t')]\rangle \quad (\text{S14})$$

Since the two spin components are independent in our experiment and the gas is balanced, both components have identical single-particle response functions χ , yielding

$$\chi_{\text{eff}} = (1 + \zeta^2)\chi. \quad (\text{S15})$$

This defines the effective susceptibility χ_{eff} that replaces χ in the single-component threshold condition Eq. S9, yielding to the threshold equation

$$\chi = \frac{1}{2D_{0c}(1 + \zeta^2)}. \quad (\text{S16})$$

3. Polarization effects

The transverse pump is linearly polarized perpendicular to both the cavity axis and the magnetic field. In our parameter regime, the Zeeman splitting is non negligible compared to the detuning between the cavity resonance and the σ_- transition. As a result, the contributions of the σ_- and σ_+ polarizations to the light-matter coupling must be treated separately.

The Hamiltonian can then be written as

$$\hat{H} = \tilde{\Delta}_p \hat{a}^\dagger \hat{a} - \left(\frac{g_{\uparrow,+}\Omega_{\uparrow,+}}{2\Delta_{\uparrow,+}} + \frac{g_{\uparrow,-}\Omega_{\uparrow,-}}{2\Delta_{\uparrow,-}} \right) (\hat{\theta}_\uparrow + \zeta \hat{\theta}_\downarrow) (\hat{a}^\dagger + \hat{a}), \quad (\text{S17})$$

with

$$\zeta = \frac{\frac{g_{\downarrow,+}\Omega_{\downarrow,+}}{2\Delta_{\downarrow,+}} + \frac{g_{\downarrow,-}\Omega_{\downarrow,-}}{2\Delta_{\downarrow,-}}}{\frac{g_{\uparrow,+}\Omega_{\uparrow,+}}{2\Delta_{\uparrow,+}} + \frac{g_{\uparrow,-}\Omega_{\uparrow,-}}{2\Delta_{\uparrow,-}}}. \quad (\text{S18})$$

Here, the subscripts \uparrow, \downarrow refer to the spin species, while $+, -$ to the polarization components of the light. Solving the linearized equations of motion yields the threshold condition

$$\chi = \frac{\tilde{\Delta}_p^2 + (\kappa/2)^2}{\tilde{\Delta}_p \left(\frac{g_{\uparrow,+}\Omega_{\uparrow,+}}{2\Delta_{\uparrow,+}} + \frac{g_{\uparrow,-}\Omega_{\uparrow,-}}{2\Delta_{\uparrow,-}} \right)^2 (1 + \zeta^2)}. \quad (\text{S19})$$

This equation provides the quantitative relation between the experimentally measured threshold and the single-component susceptibility χ calculated from first principles, with all polarization and coupling asymmetries taken into account. In practice, the σ_+ transition is detuned by 1 and 2 GHz more than the σ_- transition, depending on the magnetic field, such that its contribution is below 5% of the total light-matter coupling.

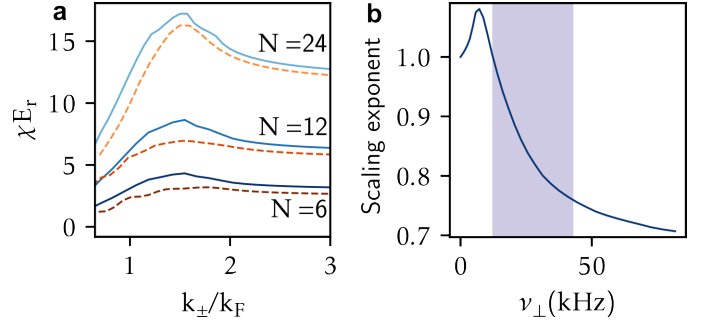


FIG. S3. (a) Susceptibility for a single-specie Fermi gas calculated using the local density approximation (solid lines) and the exact eigenstates of the harmonic trap (dashed lines) for different atom numbers. (b) Scaling exponent α of the superradiant threshold $V_{0c} \propto N^{\alpha}$, as a function of the perpendicular trap frequency, calculated using the local density approximation. For weak trap depth, we recover the bosonic scaling $\propto N$. As the trap depth is increased, we observe Fermi pressure effects, such as a super-scaling of the threshold with atom number, showing the availability of many low-energy excitations near the Fermi surface, and a sub-scaling at high trap frequencies due to Pauli blocking. The shaded region corresponds to the parameter range explored in Figure 3.

E. Simulations of the density-density response function

To predict the phase boundary between the normal and superradiant phases, we calculate the zero-frequency density-density response function defined in Equations S7-S8. In this work, we evaluate χ using (I) plane-wave eigenstates in the local density approximation (LDA) and (II) the exact harmonic oscillator eigenstates.

1. Local density approximation

The susceptibility defined in Eq. S8 describes the response of the operator $\hat{\theta}$ to a perturbation $\hat{\theta}$ in the context of linear response theory [63]. To calculate the commutator, we can express the density wave operator from Eq. S3 as

$$\hat{\theta} = \frac{1}{4} \sum_{\mathbf{k}=\pm\mathbf{k}_{\pm}} \int d\mathbf{r} \hat{n}(\mathbf{r}) e^{i\mathbf{k}\mathbf{r}} = \frac{1}{4} \sum_{\mathbf{k}=\pm\mathbf{k}_{\pm}} \hat{n}_{\mathbf{k}}, \quad (\text{S20})$$

where $\hat{n}_{\mathbf{k}}$ is the Fourier transform of the density operator $\hat{n}_{\mathbf{k}} = \int d\mathbf{r} \hat{n}(\mathbf{r}) e^{i\mathbf{k}\mathbf{r}}$. The commutator between $\hat{\theta}$ operators can be expressed in the more familiar commutator between density fluctuations writing

$$[\hat{\theta}(t), \hat{\theta}(0)] = \frac{1}{16} \sum_{\mathbf{k}=\pm\mathbf{k}_{\pm}} [\hat{n}_{\mathbf{k}}(t), \hat{n}_{\mathbf{k}}(0)], \quad (\text{S21})$$

which implies an averaging of the response over the different wavevectors of the perturbation. To calculate the response in the local density approximation, we divide the 3D harmonic trap into small homogeneous volumes \mathcal{V} . The trap is treated as locally flat and the eigenstates in each volume are

approximated by plane waves. In each volume, the response of the gas is isotropic, meaning that Eq. S21 becomes

$$[\hat{\theta}(t), \hat{\theta}(0)] = \frac{1}{4} [\hat{n}_{\mathbf{k}_\pm}(t), \hat{n}_{\mathbf{k}_\pm}(0)], \quad (\text{S22})$$

where we have defined $\mathbf{k}_\pm = |\pm \mathbf{k}_\pm|$. For plane waves eigenstates, the susceptibility per unit volume is [33, 64]

$$\tilde{\chi}_V(\mathbf{k}) = \frac{1}{4} \frac{m}{2\pi^2 \hbar^2 \mathbf{k}} \int_0^\infty q n_F^V(q, \mu_V) \log \left| \frac{k+2q}{k-2q} \right| dq. \quad (\text{S23})$$

The total susceptibility of a Fermi gas is obtained by summing the susceptibility density over all volumes:

$$\chi(\mathbf{k}) = \sum_V \tilde{\chi}_V(\mathbf{k}) \cdot \mathcal{V}, \quad (\text{S24})$$

\mathcal{V} the box volume. At zero temperature, the right-hand part of the Eq. S23 simplifies to the Lindhard function. To calculate this quantity at finite temperature, we need to know the local chemical potential for each volume μ_V , which enters the Fermi-Dirac distribution

$$n_F^V(q, \mu_V) = \frac{1}{e^{\beta(\frac{\hbar^2 q^2}{2m} - \mu_V)} + 1}. \quad (\text{S25})$$

The chemical potential in each volume is determined by matching the atom number obtained from integrating the Fermi-Dirac distribution over energy (Eq. S26) to the local atom number set by the harmonic trap profile (Eq. S28). The first term is given by

$$N_V = \frac{\hbar^2}{m} \int_0^\infty q g(q) n_F^V(q, \mu_V) dq \quad (\text{S26})$$

$$g(q) = \frac{\mathcal{V}}{4\pi^2} \left(\frac{2m}{\hbar^2}\right)^{3/2} \sqrt{\frac{\hbar^2 q^2}{2m}} \quad (\text{S27})$$

where $g(q)$ is the density of states of the 3D box. The second term is obtained considering a volume centered at $\mathbf{r} = (\bar{x}, \bar{y}, \bar{z})$. Its atom number is given by

$$N_V = n(\mathbf{r}) \mathcal{V} \quad (\text{S28})$$

with $n(\mathbf{r}) = -\frac{1}{\lambda_{dB}^3} \text{Li}_{3/2}(-e^{\beta(\mu - U(\mathbf{r}))})$ the atomic distribution in the harmonic trap. Here, $U(\mathbf{r})$ the trap harmonic potential, λ_{dB} the thermal deBroglie wavelength of the cloud, $\text{Li}_{3/2}$ is the polylogarithm function, $\beta = 1/k_B T$. The total chemical potential μ of the harmonic trap is fixed by the total atom number.

2. Exact harmonic oscillator eigenstates

Equation S8 can also be evaluated using the exact eigenstates of the tweezer trap, which are Hermite-Gauss functions denoted as $\Psi_i(\mathbf{r})$. Using Wick's theorem to evaluate

the expectation values of the Fermionic operators, Eq. S8 becomes [65]:

$$\chi = \sum_{ij} \left| \langle \Psi_i(\mathbf{r}) | \cos \mathbf{k}_c \mathbf{r} \cos \mathbf{k}_p \mathbf{r} | \Psi_j(\mathbf{r}) \rangle \right|^2 \frac{n_F(E_i) - n_F(E_j)}{E_i - E_j} \quad (\text{S29})$$

where $\mathbf{i} = (n_x, n_y, n_z)$ denotes the 3D harmonic oscillator states, $\Psi_i(\mathbf{r}) = \Psi_{n_x}(x) \Psi_{n_y}(y) \Psi_{n_z}(z)$, $E_i = E(n_x) + E(n_y) + E(n_z)$ are the eigenenergies and n_F the Fermi-Dirac distribution.

This formula is fully general, and the Lindhard function for homogeneous systems is retrieved upon replacing the eigenstates by plane waves and turning the sum into an integral. It suggests that the susceptibility, hence the superradiant transition can be suppressed by two mechanisms: (i) at high momentum, the energy denominator is given by the recoil, yielding the overall $1/E_r$ scaling observed in Bose-Einstein condensates (see Fig.2c), and (ii) at low momentum where states are equally occupied the Fermi distributions at the numerator cancel each other, a manifestation of Pauli blocking. Note that at higher temperature the suppression can also persist in the low momentum regime when the two (thermal) distributions are very similar, which happens when the temperature is much higher than the recoil in the classical gas.

Denoting the trap aspect ratio $r = \omega_\perp / \omega_\parallel$, with $\omega_\perp, \omega_\parallel$ respectively the perpendicular and longitudinal trap frequencies, the susceptibility at zero temperature reads

$$\chi = \frac{1}{\hbar \omega_\parallel} \sum_{\substack{n_x, n_z \\ n'_x, n'_z \\ n_y}} \frac{\Upsilon(E_F - E_{n_x, n_y, n_z}) - \Upsilon(E_F - E_{n'_x, n_y, n'_z})}{(n'_x - n_x) + r(n'_z - n_z)} \left| \int dx \Psi_{n_x}(x) \Psi_{n'_x}(x) \cos(k_c x) \right|^2 \left| \int dz \Psi_{n_z}(z) \Psi_{n'_z}(z) \cos(k_p z) \right|^2, \quad (\text{S30})$$

where $E_{n_x, n_y, n_z} = \hbar \omega_\parallel (n_x + 1/2) + \hbar \omega_\perp (n_y + n_z + 1)$. This expression can only be calculated at fixed Fermi energy, so different atom numbers can give the same result depending on the shell filling of the anisotropic harmonic trap. The main difficulty of the numerical evaluation of Eq. S30 is to ensure the convergence of the integrals as a function of the maximal number of states considered. We verified convergence at zero temperature by varying the maximum number of Hermite functions in each direction. For the results presented in Figure 2, having 24 atoms in each spin component, which means $E_F = 17 \hbar \omega_\parallel$, we used $N_\parallel = 175$ states along the longitudinal direction and $N_\perp = N_\parallel / r$ for the transverse directions.

3. Comparison between the two simulations

Figure S3a shows the susceptibility calculated using LDA and exact harmonic oscillator eigenstates. Both methods reproduce the qualitative shape of the curve and capture the $1/k^2$ dependence of the low trap depth regime. Quantitative differences appear at the peak, where the exact shape of the

eigenstates has the biggest effect. In the high trap depth regime ($k/k_F < 1$), the local density approximation is not valid as the trap potential varies significantly over the length of the Fermi wavevector. The discrepancy in the asymptotic behavior at high momentum is due to the difference between the Fermi energy of the anisotropic harmonic oscillator and the LDA. LDA captures the continuous variation between the shell filling effects of the exact eigenstates calculations but neglects the finite-size effects of the trap. For instance, the largest transverse trap frequencies explored in Figure 2 represents $1.7E_r$, approaching the Lamb-Dicke regime. For the parameters studied here, the exact eigenstates calculation provides the most accurate description of shell-dependent features, while LDA gives a reliable approximation for larger atom numbers and large momentum or when smoothing over closed-shell effects.

Importantly, in the grand-canonical ensemble the atom number varies in discrete steps, preventing the description of open shells. Accurate calculations in the canonical ensemble require directly manipulating Slater determinants, as done recently to study shell filling effects in light-matter interactions [22].

4. Atom number scaling

The LDA simulation of the susceptibility allows us to track the scaling of the superradiant phase boundary with atom number. Fig. S3b shows the scaling exponent α , extracted from the simulation for our system geometry, as a function of the square root of the perpendicular trap frequency for a zero-temperature Fermi gas. For shallow traps, $\alpha \rightarrow 1$, corresponding to the non-Pauli-blocked regime. As the trap frequency increases, Pauli blocking reduces the scaling exponent, which eventually reaches a plateau around $\alpha \simeq 0.7$. Notably, there exists an intermediate regime where the exponent exceeds unity, likely reflecting the enhanced availability of low-energy density excitations near the Fermi

surface and confirming that Fermi pressure can indeed assist self-organization. The shaded region in the figure indicates the range of trap frequencies explored experimentally.

5. Magnetic superradiance and effect of the interactions

In Figure 4 we consider a situation where the cavity is red-detuned from one spin state and blue-detuned from the other. Considering $g_\uparrow = g_\downarrow = g$, $\Omega_\uparrow = \Omega_\downarrow = \Omega$ and $\Delta_\downarrow = \Delta = -\Delta_\uparrow$, this Hamiltonian can be written as

$$\hat{H} = \tilde{\Delta}_p \hat{a}^\dagger \hat{a} - \frac{g\Omega}{2\Delta} (\hat{\theta}_\downarrow - \hat{\theta}_\uparrow) (\hat{a} + \hat{a}^\dagger) \quad (\text{S31})$$

The cavity field couples to the operator

$$\hat{\Theta} = \hat{\theta}_\downarrow - \hat{\theta}_\uparrow = \int d\mathbf{r} \cos(\mathbf{k}_c \cdot \mathbf{r}) \cos(\mathbf{k}_p \cdot \mathbf{r}) (\hat{n}_\downarrow(\mathbf{r}) - \hat{n}_\uparrow(\mathbf{r})), \quad (\text{S32})$$

determined by the magnetization density of the gas. In the superradiant phase, the two spin species redistribute to the maxima and minima of the interference pattern, thus creating a density modulation with a spin-wave character. The spin susceptibility is calculated as

$$\chi_s(t-t') = -i\chi(t-t') \langle [\hat{\theta}_\uparrow(t) - \hat{\theta}_\downarrow(t), \hat{\theta}_\uparrow(t') - \hat{\theta}_\downarrow(t')] \rangle, \quad (\text{S33})$$

which differs from the density susceptibility χ_{eff} defined above (Eq. S14) by the minus signs. The equation for the threshold remains unaltered for the non-interacting case

$$\chi_s = 2\chi = \frac{1}{2D_{0c}}. \quad (\text{S34})$$

For the measurement of Fig. 4d, $k \sim 0.5 k_F$, a regime at the edge of the validity of the local density approximation. The number of atoms is however too large to run the exact eigenstates simulation until convergence.